

# Subgrain $^{40}\text{Ar}/^{39}\text{Ar}$ dating of museum-quality micas reveals intragrain heterogeneity

M.O. Naumenko-Dèzes<sup>a,\*</sup>, I.M. Villa<sup>b,c</sup>, Y. Rolland<sup>a,d</sup>, S. Gallet<sup>a</sup>, P. Lanari<sup>b</sup>

<sup>a</sup> Université Côte d'Azur, CNRS, OCA, IRD, Géoazur, 250 rue Albert Einstein, Sophia Antipolis, 06560 Valbonne, France

<sup>b</sup> Institut für Geologie, Universität Bern, 3012 Bern, Switzerland

<sup>c</sup> Centro Universitario Datazioni e Archeometria, Università di Milano Bicocca, 20126 Milano, Italy

<sup>d</sup> EDYTEM, Université Savoie Mont Blanc, CNRS, UMR 5204, 73370 Le Bourget-du-Lac, France

## ARTICLE INFO

### Keywords:

$^{40}\text{Ar}/^{39}\text{Ar}$  dating

$^{40}\text{K}$  half-life

Geological intercalibration

Retrogression reactions

## ABSTRACT

Museum-grade mica megacrysts of the Phalaborwa phlogopite (ca. 2 Ga) and the Rubikon pegmatite (ca. 0.5 Ga) were screened for intra-grain compositional and chronological heterogeneities by electron probe microanalysis and  $^{40}\text{Ar}/^{39}\text{Ar}$  dating, respectively. Both micas were known to have Rb—Sr ages indistinguishable from U—Pb ages. Even though step heating plateaus were obtained for nearly a hundred 100  $\mu\text{m}$  scale subgrain chips, age variations of several percents were observed among individual chips. The age variations were unrelated to the position within the megacryst and to the position in the irradiation canister. Element mapping parallel and perpendicular to the (001) plane showed significant variations in concentrations of major elements Ti, Fe, Mn, K, Al. Cation transport, element redistribution and retrograde mineral formation that escaped visual detection require open-system, fluid-assisted chemical reactions. These recrystallization processes occurred during one or several post-magmatic hydrothermal event(s). The spatial distribution of sub-grain ages show that  $^{40}\text{Ar}/^{39}\text{Ar}$  dating does not provide a simple, diffusion-controlled cooling age, but rather apparent ages controlled by mineral retrogression and recrystallization. The result was variable loss of Ar at the subgrain scale. These observations show that retrogression events cannot be detected by the presence or absence of plateau ages. Instead, recrystallization can be diagnosed (1) by a thorough petrological investigation based on microchemical maps, and (2) by Cl/K and Ca/K constraints from  $^{40}\text{Ar}/^{39}\text{Ar}$  systematics. The quest for a natural mineral sufficiently homogeneous to act as a precise calibrator for the  $^{40}\text{K}$  half-life remains unsatisfactory.

## 1. Introduction

Three main issues are currently limiting the accuracy and precision of the  $^{40}\text{Ar}/^{39}\text{Ar}$  dating technique and consequently its reliability: (1) the systematic uncertainty of the flux monitor ages (e.g. the Fish Canyon Tuff sanidine: Cebula et al., 1986; Rivera et al., 2011), which can be due at least partly due to mineralogical inhomogeneities (e.g. Bachmann et al., 2002); (2) the lack of understanding of the intra-grain  $^{40}\text{Ar}/^{39}\text{Ar}$  age distribution; (3) the uncertainty on the  $^{40}\text{K}$  decay constant and its branching ratio (Steiger and Jäger, 1977; Naumenko-Dèzes et al., 2018).

Issue (3) could, at least in principle, be solved by geological intercalibration: the age determination of a suitable calibrator sample by two or more geochronometric systems yields the unknown decay constant(s) as a function of one decay constant taken as a reference (usually that of  $^{238}\text{U}$ ), provided the calibrator records a “point-like” geological history

(Begemann et al., 2001) and is homogeneous within the analytical resolution (JCGM, 2008, entry F.2.6.2). This is a long-standing problem inherent in intercalibration experiments (Villa et al., 2016, 2020). The metrological requirement reveals a contradiction with the natural heterogeneity of many natural samples and their un-point-like extensive retrograde reaction history. For the calibrators of the  $^{40}\text{K}$  decay half-life the scarcity of chemically homogeneous samples has been addressed by Naumenko-Dèzes et al. (2018). The two least ill-preserved samples analyzed in that study were two museum-grade mica megacrysts: the Phalaborwa phlogopite (ca. 2 Ga old), and the Rubikon lepidolite (ca. 0.5 Ga old), which were dated by Rb—Sr and K—Ca. The Rb—Sr age of both samples (calculated with the  $^{87}\text{Rb}$  decay constant recommended by Villa et al. (2015)) agreed with the independently known U—Pb ages. This is strong evidence that the Rb—Sr system records no significant post-magmatic perturbation. In contrast, the K—Ca ages, when calculated using the Steiger and Jäger

\* Corresponding author at: French Geological Survey, BRGM, 3 Avenue Claude Guillemin, 45100 Orléans, France.

E-mail address: [marie@geosphere.ch](mailto:marie@geosphere.ch) (M.O. Naumenko-Dèzes).

<https://doi.org/10.1016/j.chemgeo.2021.120215>

Received 21 October 2020; Received in revised form 27 March 2021; Accepted 1 April 2021

Available online 3 April 2021

0009-2541/© 2021 Elsevier B.V. All rights reserved.

(1977) decay constant ( $\lambda_{40}$ ) and branching ratio (B), were apparently younger than the U—Pb age. However, by analogy with the Rb—Sr system, the K—Ca system is expected to record the same lack of detectable chemical retrogression, as both systems feature alkali parents and earth alkali daughters. Therefore, Naumenko-Dèzes et al. (2018) interpreted the apparent age discordance as a constraint for a ( $\lambda_{40}$ , B) pair different from that proposed by Steiger and Jäger (1977). An additional complication was that Dèzes (2016) had obtained preliminary apparent K—Ar ages in disagreement with all of the above ages. One reason for the discordance could be if diffusive loss of Ar\* had occurred and had been faster than that of Sr\* and Ca\*. Such an effect for the Madagascar sanidine had been hypothesized by Nägler and Villa (2000), and documented by Flude et al. (2014). Another reason could have been compositional heterogeneities (near the resolution of EPMA analyses, approx. 1%) resulting from dissolution/reprecipitation. The spatial distribution of chemical differences resulting from these two resetting mechanisms is distinctly different (Villa, 2016): diffusion necessarily produces a bell-shaped concentration profile, whereas recrystallization usually results in patchy zonation.

This study endeavours to assess the above-mentioned limiting factors by exploring the spatial distribution of the radiogenic  $^{40}\text{Ar}$  ( $^{40}\text{Ar}^*$ ) and  $^{40}\text{K}$  concentrations using high precision  $^{40}\text{Ar}/^{39}\text{Ar}$  dating on subgrain aliquots of the Phalaborwa and Rubikon micas studied by Naumenko-Dèzes et al. (2018). Because both samples appear fresh, it was expected that  $^{40}\text{Ar}/^{39}\text{Ar}$  ages would be regularly distributed in the grains and would thus make it possible to obtain constraints on the K—Ar and K—Ca double decay constants.

## 2. Analytical techniques

Phlogopite (Fig. 1) from the Phalaborwa layered intrusion, South Africa, was obtained from the Phalaborwa Mine Collection, courtesy K. Mezger. The Phalaborwa intrusion consists of carbonatites, phoscorite and pyroxenites. Each layer of this intrusion was dated with U—Pb; the concordant U—Pb ages indicate a rapid emplacement sequence (Wu et al., 2011). Its fast cooling was suggested as a recommendation to choose it as a  $^{40}\text{K}$  half-life calibrator (Y. Amelin, pers. comm., 2014), following the assertion by Steiger and Jäger (1977) that intercalibrations are reliable if samples look fresh and cooled quickly. Five phlogopite sheets up to a cm size were hand-picked from phoscorite. The sheets were first split along cleavage planes with a steel blade so as to obtain a thin, transparent, visually inclusion-free layer, photographed, then cut into long strips ca. 1–2 mm wide. Strips were then cut into 0.2–0.4 mm wide rectangular chips with a mass of the order of 0.1 mg, recording and photographing the position of each of them within the

original grain. The mica rectangles were individually packed into thin, high purity aluminum foil disks that were stacked in an aluminum tube interspaced with interlaboratory age monitors and with the Rubikon lepidolite (see below) for irradiation (Fig. 2). The mass of the thin rectangular pieces was about 10 times larger than the typical UV Laser microprobe sample size; in order to have  $^{37}\text{Ar}$  and  $^{38}\text{Ar}$  beams large enough for a sufficiently precise measurement, some samples consisted of larger chips or several rectangles. Rb—Sr dating on another fragment of the same hand specimen yielded an age of  $2056 \pm 5.2$  Ma (Naumenko-Dèzes et al., 2018), concordant with the U—Pb and Pb—Pb ages of baddeleyite and zircon ( $2060.3 \pm 0.4$  Ma, Kumar et al., 2014).

Lepidolite from the Rubikon complex, Namibia, was collected from a Li and Rb bearing pegmatite; a ca. 3 cm lepidolite foil was obtained from Schweizerisches Naturhistorisches Museum, Bern, courtesy B.A. Hofmann. Existing age data for Rubikon are a baddeleyite U—Pb age of  $505.5 \pm 2.7$  Ma

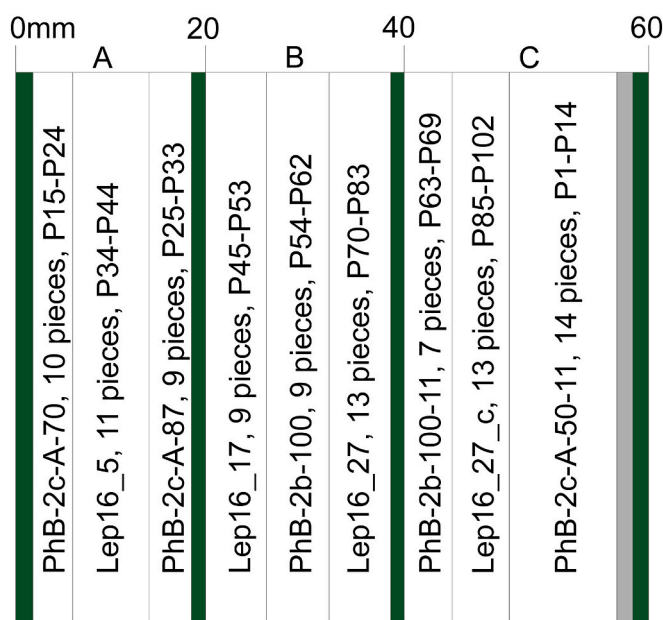


Fig. 2. Scheme of the irradiation package. Green, irradiation monitors; PhB, phlogopite; Lep, lepidolite; P1-P102, individually packed rectangular mica chips. Individual chip positions in the stack increased by approx. 0.5 mm relative to the previous one. (For interpretation of the references to colour in this figure legend, the reader is referred to the web version of this article.)

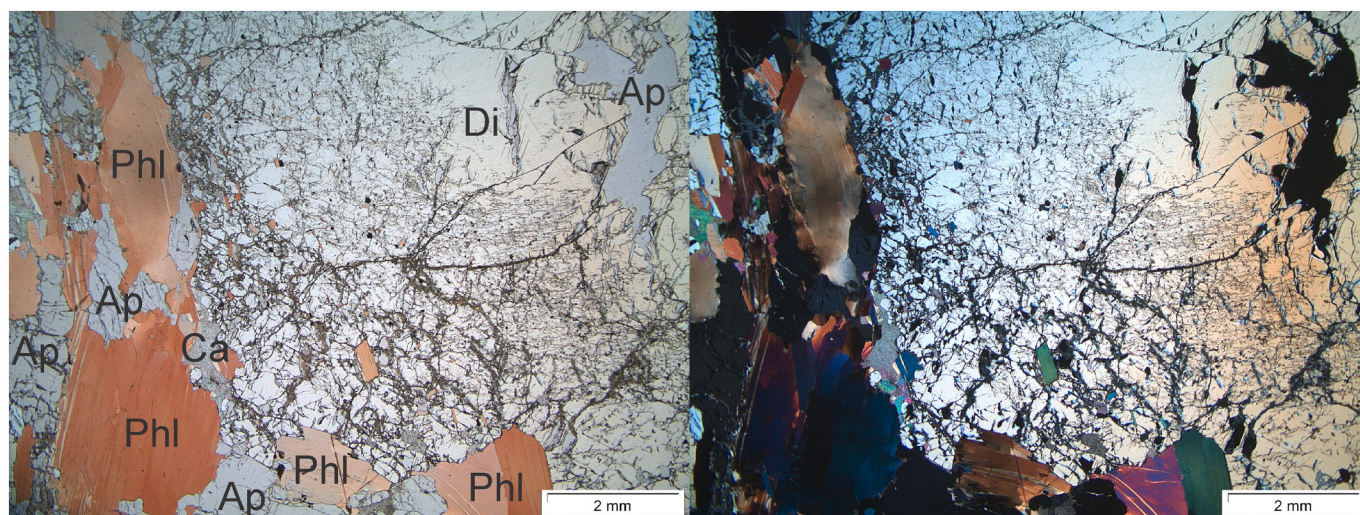


Fig. 1. Thin-section pictures of the Phalaborwa sample. Left, plane polarized light, right, cross polarized light.

(Melcher et al., 2015), coincident with the Rb—Sr age,  $504.7 \pm 4.2$  Ma (Naumenko-Dèzes et al., 2018). The lepidolite foil was first cleaved and then cut into rectangular chips in the same way as the Phalaborwa phlogopite. The chips were photographed, wrapped and irradiated in the same package as the latter. The 270 MWh irradiation was performed at McMaster University, Canada, avoiding Cd shielding in order to preserve the petrological information deriving from  $^{38}\text{Ar}_{\text{Cl}}$ . For reasons not anticipated, many samples were only measured after  $^{37}\text{Ar}_{\text{Ca}}$  had decayed.

For our purpose of charting the geometrical distribution of  $^{40}\text{Ar}^*$  in the megacryst it is sufficient to use self-monitoring, i.e., calculating the irradiation parameter  $J$  for one arbitrarily chosen chip (P97 and P67, respectively: Table 1) assumed to have a K—Ar age equal to the Rb—Sr age previously obtained by us on a different fragment of the same megacryst (Rubikon) or hand specimen (Phalaborwa). Self-monitoring circumvents the acute problem that the correct half-life of  $^{40}\text{K}$  is unknown. By referring the relative variations of the  $^{40}\text{Ar}^*/^{39}\text{Ar}$  ratio to the correct Rb—Sr age, instead of referring them to the  $^{40}\text{Ar}^*/^{39}\text{Ar}$  ratio of an irradiation monitor having a different age, the problem of taking into account the unknown curvature of the  $^{40}\text{Ar}^*/^{39}\text{Ar}$  increase with time is reduced to approximating the growth curve with a linear increase for the time interval between 2000 and 2060 Ma, or between 490 and 505 Ma. Thus, we calculated the K—Ar ages using the Steiger and Jäger (1977) constants, but the relative ages among the chips remain the same (to less than 0.1% bias) if we use any of the ( $\lambda_{40}$ , B) pairs discussed by Naumenko-Dèzes et al. (2018). If the mica were chronologically homogeneous, the apparent ages of all chips should be equal, after correcting for the smooth irradiation gradient. If the apparent ages of the pieces show an additional difference after correcting for the irradiation gradient, and this difference is due to diffusive Ar loss, then the position of the piece within the original crystal should define a bell-shaped diffusion profile. If the relationship between apparent age and position is patchy, the rejuvenation mechanism controlling the  $^{40}\text{Ar}^*$  and K distributions can only be due to an additional process faster than diffusion, such as retrograde reactions.

Both Rubikon and Phalaborwa samples were measured in two different laboratories, on two different mass spectrometers and using two different degassing protocols. In Milano Bicocca, samples were preheated to ca. 250 °C for 30 min under vacuum and then step-heated in a double-vacuum furnace and analyzed in a NuInstruments Noblesse™ mass-spectrometer equipped with one Faraday collector and two ion counters (Bosio et al., 2020). The intercalibration of the three collectors was guaranteed in each measurement, for the instantaneous source conditions, by measuring at least two isotopes on two different collectors. At Géoazur, Nice, individual chips were mounted in a drilled copper plate in a steel chamber, maintained at  $10^{-8}$ – $10^{-9}$  mbar, not preheated, and step-heated with a 100 kHz IR-CO<sub>2</sub> laser used at 5–15% power output during 60 s. Argon isotopes were measured in the multi-collector ARGUS VI spectrometer with five Faraday detectors ( $10^{11}$  Ω for  $^{40}\text{Ar}$ ,  $10^{12}$  Ω resistors for other masses). Collector gain calibration was performed by the computer-controlled application of pre-determined voltages to each collector. Collector sensitivity was controlled every week by peak jumping measurements of air pipettes and corresponding correction was applied. Over the course of one year, the relative gain drift between collectors did not exceed 19 ppm. System blanks were measured before and after each measurement. The average of these two measurements was then subtracted from the measured sample value. The blanks typically accounted for less than 0.06% of the  $^{40}\text{Ar}$ , 0.6–3.81% of the  $^{38}\text{Ar}$  and  $^{39}\text{Ar}$ , and 0.12–0.71% of the  $^{36}\text{Ar}$ . Mass discrimination for both mass spectrometers was monitored by daily analyses of air pipette volumes. Géoazur used ArArCalc© software v2.5.2 for data processing (Koppers, 2002), Milano Bicocca used a dedicated calculation spreadsheet. Spreadsheets with the complete analytical data from both laboratories can be found in Appendix A, in which  $^{40}\text{Ar}^*/^{39}\text{Ar}$  ages are calculated with fixed  $J$  (see above), but not corrected for the flux gradient. Ages in Table 1 are corrected for flux gradient.

Electron probe microanalyses (EPMA) were obtained on a JEOL 8200 electron microprobe at Institut für Geologie, Bern University, by mounting other, nearby cleavage fragments of the same megacryst parallel and perpendicularly to the (001) plane, the latter exposing the interior of the TOT phyllosilicate structure (Heri et al., 2014). The data of the EPMA analyses were calibrated with XMapTools (Lanari et al., 2014a, 2019), which allows the precise determination of mineral species at the ca. 10 μm scale (e.g., Lanari et al., 2014b). This provides petrological constraints for the interpretation of the  $^{40}\text{Ar}^*/^{39}\text{Ar}$  data. All analyzed elements (Mg, Mn, Al, Fe, Ti, Si, K) show resolvable concentration variations (Figs. 3, 4, and Appendix B).

In addition to the mica megacrysts, several interlaboratory monitors (Fish Canyon sanidine, Alder Creek sanidine, McClure Mountains amphibole) were also analyzed; mg-sized aliquots were wrapped in flat Al foil disks, whose positions were also recorded. Their chronological heterogeneity, as already documented by Jicha et al. (2016) and Naumenko-Dèzes et al. (2018), was reproduced here. The role of the interlaboratory monitors in the present experiment was minor, other than to confirm the irradiation gradient of 0.6%/cm already inferred from the self-monitoring.

### 3. Results

The apparent  $^{40}\text{Ar}^*/^{39}\text{Ar}$  ages of the lepidolite chips span a 8% interval from  $505 \pm 8$  Ma down to  $466 \pm 7$  Ma (Fig. 5, Table 1). It is important to point out that individual chip ages of Rubikon and Phalaborwa are not calibrated absolute ages; instead, they represent intracrystal variations of the  $^{40}\text{Ar}^*/^{39}\text{Ar}$  ratio normalized to one arbitrary chip (P97 and P67, respectively). The principal result is the scatter of the apparent chip ages, not their absolute value. It could be that some chips show calibrated K—Ar ages higher than the Rb—Sr and U—Pb age (due to removal of K), but more probably the highest K—Ar ages should be equal, within uncertainty, to the Rb—Sr and U—Pb age. The age variations are neither a function of the position in the irradiation canister nor of the position inside the crystal.

The apparent  $^{40}\text{Ar}^*/^{39}\text{Ar}$  ages of the phlogopite chips vary from  $206 \pm 21$  Ma down to  $1984 \pm 20$  Ma (Fig. 6, Table 1). The age variations neither correlate with the position of the chips in the crystal nor with the position of the chips in the irradiation canister (Fig. 7). The darker colored sheets showed ages reset below 2010 Ma. Two of the cleanest and thinnest sheets yielded ages close to the 2060 Ma age of the intrusion. The spatial age variation is random, a 2050 Ma chip may lie next to a 2005 Ma one. As the samples were analyzed in two laboratories, the comparison confirms that the observed age distribution is not an analytical artifact but a primary effect.

Both micas in both laboratories gave invariably “plateau” ages (Fig. 8 shows one example of two neighboring chips irradiated in adjacent positions). “Plateaus” had often been interpreted in the past as a sign of ideality. The “plateau age” variations largely exceeding the 2 sigma level imply instead that at most one of the “plateaus” can reflect ideal behaviour, whereas all others do not. This reproduces results obtained by Foland (1983) and Popov et al. (2019), calling into question the identification of “plateaus” with sample ideality. Therefore, the questions should be: what brings about the observed variations, what diagnostic tools does the  $^{40}\text{Ar}^*/^{39}\text{Ar}$  systematics provide, what correction (if any) can be applied, and what do our findings imply for the viability of micas as precise half-life calibrators?

The observed chronological patchiness of the two museum megacrysts required further petrological investigations. Electron probe microanalysis of the mica mounts showed clear variations in major element concentrations (Figs. 3–4): an almost tripling of TiO<sub>2</sub> (from 0.6 to 1.6%) and relative increases around 20% of FeO (between 7.5 and 9.5%) and MnO (between 1.8 and 2.1%). Some schlieren-like variations of K, Al and Mn concentrations were observed in the (001) plane of the lepidolite (Fig. 3), unrelated to visible microfractures. The variations in the plane perpendicular to (001) were even more revealing. Cleavage

**Table 1**  
<sup>40</sup>Ar/<sup>39</sup>Ar ages of the chips of Phalaborwa phlogopite (PhB) and Rubikon lepidolite (Lep).

Sample	Sample N	Mineral	Location	<sup>40</sup> Ar/ <sup>39</sup> Ar age	± 2σ (Ma)	± 2σ %	<sup>40</sup> Ar/ <sup>39</sup> Ar_age/Rb-Sr_age	± 2σ (Ma) (incl. J uncert.)	Irradiation position	Method	Measurement Lab
PhB-2c-A-50	P1	phlogopite	Phalaborwa	2013	21	1.02	0.979	0.010	52.8	Step heating	Nice Sophia Antipolis
PhB-2c-A-50	P2	phlogopite	Phalaborwa	2028	21	1.02	0.986	0.011	53.6	Step heating	Nice Sophia Antipolis
PhB-2c-A-50	P3	phlogopite	Phalaborwa	2025	20	1.01	0.985	0.010	54.4	Step heating	Nice Sophia Antipolis
PhB-2c-A-50	P4	phlogopite	Phalaborwa	2052	21	1.03	0.998	0.011	55.2	Step heating	Nice Sophia Antipolis
PhB-2c-A-50	P5	phlogopite	Phalaborwa	2004	20	1.02	0.974	0.010	56.0	Step heating	Nice Sophia Antipolis
PhB-2c-A-50	P6	phlogopite	Phalaborwa	1979	20	1.02	0.962	0.011	56.9	Step heating	Nice Sophia Antipolis
PhB-2c-A-50	P7	phlogopite	Phalaborwa	2032	21	1.03	0.989	0.011	57.7	Step heating	Nice Sophia Antipolis
PhB-2c-A-50	P8	phlogopite	Phalaborwa	2005	21	1.03	0.975	0.011	58.5	Step heating	Nice Sophia Antipolis
PhB-2c-A-50	P9	phlogopite	Phalaborwa	2035	21	1.01	0.990	0.010	59.3	Step heating	Nice Sophia Antipolis
PhB-2c-A-50	P10	phlogopite	Phalaborwa	2001	21	1.04	0.973	0.011	60.1	Step heating	Nice Sophia Antipolis
PhB-2c-A-50	P11	phlogopite	Phalaborwa	2023	21	1.03	0.984	0.011	61.0	Step heating	Nice Sophia Antipolis
PhB-2c-A-50	P12	phlogopite	Phalaborwa	1985	20	1.03	0.966	0.011	61.8	Step heating	Nice Sophia Antipolis
PhB-2c-A-50	P13	phlogopite	Phalaborwa	2037	17	0.83	0.991	0.009	62.6	Step heating	Milano
PhB-2c-A-50	P14	phlogopite	Phalaborwa	2024	18	0.89	0.984	0.009	63.4	Step heating	Milano
<b>Weighted average age (Isoplot)</b>			<b>MSWD = 4.2</b>	<b>2018</b>	<b>12</b>	<b>0.59</b>					
PhB-2c-A-70	P15	phlogopite	Phalaborwa	2059	24	1.17	1.002	0.012	2.4	Step heating	Nice Sophia Antipolis
PhB-2c-A-70	P16	phlogopite	Phalaborwa	2066	21	1.03	1.005	0.011	2.8	Step heating	Nice Sophia Antipolis
PhB-2c-A-70	P17	phlogopite	Phalaborwa	2056	21	1.03	1.000	0.011	3.2	Step heating	Nice Sophia Antipolis
PhB-2c-A-70	P18	phlogopite	Phalaborwa	2011	21	1.04	0.978	0.011	3.6	Step heating	Nice Sophia Antipolis
PhB-2c-A-70	P19	phlogopite	Phalaborwa	2034	21	1.03	0.989	0.011	4.0	Step heating	Nice Sophia Antipolis
PhB-2c-A-70	P20	phlogopite	Phalaborwa	2003	21	1.04	0.974	0.011	4.4	Step heating	Nice Sophia Antipolis
PhB-2c-A-70	P21	phlogopite	Phalaborwa	2007	21	1.04	0.976	0.011	4.8	Step heating	Nice Sophia Antipolis
PhB-2c-A-70	P22	phlogopite	Phalaborwa	2009	21	1.04	0.977	0.011	5.2	Step heating	Nice Sophia Antipolis
PhB-2c-A-70	P23	phlogopite	Phalaborwa	2055	21	1.03	1.000	0.011	5.6	Step heating	Nice Sophia Antipolis
PhB-2c-A-70	P24	phlogopite	Phalaborwa	2025	28	1.38	0.985	0.014	6.0	Step heating	Milano
<b>Weighted average age (Isoplot)</b>			<b>MSWD = 5.4</b>	<b>2032</b>	<b>18</b>	<b>0.89</b>					
PhB-2c-A-87	P25	phlogopite	Phalaborwa	2026	21	1.03	0.986	0.011	14.5	Step heating	Nice Sophia Antipolis
PhB-2c-A-87	P26	phlogopite	Phalaborwa	1987	21	1.04	0.966	0.011	15.0	Step heating	Nice Sophia Antipolis
PhB-2c-A-87	P27	phlogopite	Phalaborwa	1988	21	1.04	0.967	0.011	15.5	Step heating	Nice Sophia Antipolis
PhB-2c-A-87	P28	phlogopite	Phalaborwa	2002	21	1.03	0.974	0.011	16.0	Step heating	Nice Sophia Antipolis
PhB-2c-A-87	P29	phlogopite	Phalaborwa	1988	21	1.03	0.967	0.011	16.5	Step heating	Nice Sophia Antipolis
PhB-2c-A-87	P30	phlogopite	Phalaborwa	1988	21	1.03	0.967	0.011	17.0	Step heating	Nice Sophia Antipolis
PhB-2c-A-87	P31	phlogopite	Phalaborwa	2004	21	1.03	0.975	0.011	17.5	Step heating	Nice Sophia Antipolis
PhB-2c-A-87	P32	phlogopite	Phalaborwa	2000	18	0.90	0.973	0.009	18.0	Step heating	Milano
PhB-2c-A-87	P33	phlogopite	Phalaborwa	2051	17	0.83	0.997	0.009	18.5	Step heating	Milano
<b>Weighted average age (Isoplot)</b>				<b>2006</b>	<b>18</b>	<b>0.90</b>					

(continued on next page)

Table 1 (continued)

Sample	Sample N	Mineral	Location	$^{40}\text{Ar}/^{39}\text{Ar}$ age	$\pm 2\sigma$ (Ma)	$\pm 2\sigma$ %	$^{40}\text{Ar}/^{39}\text{Ar}$ age/ Rb-Sr age	$\pm 2\sigma$ (Ma) (incl. J uncert.)	Irradiation position	Method	Measurement Lab
				<b>MSWD = 5.6</b>							
Lep-16-5	P34	lepidolite	Rubikon	488	2	0.43	0.967	0.009	6.7	Total fusion	Nice Sophia Antipolis
Lep-16-5	P35	lepidolite	Rubikon	496	9	1.86	0.982	0.020	7.4	Step heating	Nice Sophia Antipolis
Lep-16-5	P36	lepidolite	Rubikon	494	8	1.63	0.978	0.018	8.2	Step heating	Nice Sophia Antipolis
Lep-16-5	P37	lepidolite	Rubikon	493	2	0.38	0.977	0.009	8.9	Total fusion	Nice Sophia Antipolis
Lep-16-5	P38	lepidolite	Rubikon	497	2	0.38	0.986	0.009	9.6	Total fusion	Nice Sophia Antipolis
Lep-16-5	P39	lepidolite	Rubikon	483	7	1.54	0.956	0.018	10.3	Step heating	Nice Sophia Antipolis
Lep-16-5	P40	lepidolite	Rubikon	492	7	1.52	0.975	0.017	11.0	Step heating	Nice Sophia Antipolis
Lep-16-5	P41	lepidolite	Rubikon	482	8	1.56	0.955	0.018	11.8	Step heating	Nice Sophia Antipolis
Lep-16-5	P42	lepidolite	Rubikon	487	8	1.69	0.966	0.019	12.5	Step heating	Nice Sophia Antipolis
Lep-16-5	P43	lepidolite	Rubikon	486	8	1.61	0.963	0.018	13.2	Step heating	Nice Sophia Antipolis
Lep-16-5	P44	lepidolite	Rubikon	481	7	1.53	0.954	0.017	14.0	Step heating	Nice Sophia Antipolis
<b>Weighted average age (Isoplot)</b>				<b>MSWD = 7.4</b>	<b>492</b>	<b>3</b>	0.63				
Lep-16-17	P45	lepidolite	Rubikon	498	8	1.51	0.986	0.017	20.8	Step heating	Nice Sophia Antipolis
Lep-16-17	P46	lepidolite	Rubikon	475	7	1.52	0.941	0.017	21.6	Step heating	Nice Sophia Antipolis
Lep-16-17	P47	lepidolite	Rubikon	494	8	1.54	0.978	0.017	22.3	Step heating	Nice Sophia Antipolis
Lep-16-17	P48	lepidolite	Rubikon	483	7	1.54	0.957	0.018	23.0	Step heating	Nice Sophia Antipolis
Lep-16-17	P49	lepidolite	Rubikon	482	7	1.52	0.954	0.017	23.7	Step heating	Nice Sophia Antipolis
Lep-16-17	P50	lepidolite	Rubikon	479	7	1.54	0.950	0.018	24.4	Step heating	Nice Sophia Antipolis
Lep-16-17	P51	lepidolite	Rubikon	483	7	1.52	0.956	0.017	25.1	Step heating	Nice Sophia Antipolis
Lep-16-17	P52	lepidolite	Rubikon	488	8	1.54	0.967	0.018	25.8	Step heating	Nice Sophia Antipolis
Lep-16-17	P53	lepidolite	Rubikon	467	7	1.55	0.925	0.018	26.5	Step heating	Nice Sophia Antipolis
<b>Weighted average age (Isoplot)</b>				<b>MSWD = 6.4</b>	<b>483</b>	<b>7</b>	1.49				
PhB-2b-100	P54	phlogopite	Phalaborwa	1993	21	1.03	0.970	0.011	27.3	Step heating	Nice Sophia Antipolis
PhB-2b-100	P55	phlogopite	Phalaborwa	2004	21	1.03	0.975	0.011	28.0	Step heating	Nice Sophia Antipolis
PhB-2b-100	P56	phlogopite	Phalaborwa	1978	20	1.03	0.962	0.011	28.7	Step heating	Nice Sophia Antipolis
PhB-2b-100	P57	phlogopite	Phalaborwa	2008	21	1.03	0.977	0.011	29.4	Step heating	Nice Sophia Antipolis
PhB-2b-100	P58	phlogopite	Phalaborwa	1984	20	1.03	0.965	0.011	30.2	Step heating	Nice Sophia Antipolis
PhB-2b-100	P59	phlogopite	Phalaborwa	1986	21	1.03	0.966	0.011	30.9	Step heating	Nice Sophia Antipolis
PhB-2b-100	P60	phlogopite	Phalaborwa	2013	21	1.03	0.979	0.011	31.6	Step heating	Nice Sophia Antipolis
PhB-2b-100	P61	phlogopite	Phalaborwa	1988	20	1.03	0.967	0.011	32.3	Step heating	Nice Sophia Antipolis
PhB-2b-100	P62	phlogopite	Phalaborwa	1985	11	0.55	0.966	0.006	33.0	Step heating	Milano
<b>Weighted average age (Isoplot)</b>				<b>MSWD = 1.6</b>	<b>1992</b>	<b>9</b>	0.44				
PhB-2b-100-11	P63	phlogopite	Phalaborwa	2053	21	1.01	0.999	0.010	41.7	Step heating	Nice Sophia Antipolis
	P64	phlogopite	Phalaborwa	2013	21	1.03	0.979	0.011	42.4	Step heating	Nice Sophia Antipolis

(continued on next page)

Table 1 (continued)

Sample	Sample N	Mineral	Location	$^{40}\text{Ar}/^{39}\text{Ar}$ age	$\pm 2\sigma$ (Ma)	$\pm 2\sigma$ %	$^{40}\text{Ar}/^{39}\text{Ar}$ age/ Rb-Sr age	$\pm 2\sigma$ (Ma) (incl. J uncert.)	Irradiation position	Method	Measurement Lab
PhB-2b-100-11											
PhB-2b-100-11	P65	phlogopite	Phalaborwa	2029	19	0.94	0.987	0.010	43.1	Step heating	Nice Sophia Antipolis
PhB-2b-100-11	P66	phlogopite	Phalaborwa	2058	21	1.02	1.001	0.010	43.8	Step heating	Nice Sophia Antipolis
PhB-2b-100-11	P67	phlogopite	Phalaborwa	2056	21	1.01	1.000	0.010	44.5	Step heating	Nice Sophia Antipolis
PhB-2b-100-11	P68	phlogopite	Phalaborwa	2049	21	1.03	0.997	0.011	45.2	Step heating	Nice Sophia Antipolis
PhB-2b-100-11	P69	phlogopite	Phalaborwa	2036	21	1.02	0.990	0.010	46.0	Step heating	Nice Sophia Antipolis
<b>Weighted average age (Isoplot)</b>			<b>MSWD = 3.1</b>	<b>2042</b>	<b>16</b>	<b>0.78</b>					
Lep-16-27	P70	lepidolite	Rubikon	466	7	1.51	0.924	0.017	33.5	Step heating	Nice Sophia Antipolis
Lep-16-27	P71	lepidolite	Rubikon	474	7	1.56	0.939	0.018	34.0	Step heating	Nice Sophia Antipolis
Lep-16-27	P72	lepidolite	Rubikon	466	7	1.51	0.923	0.017	34.5	Step heating	Nice Sophia Antipolis
Lep-16-27	P73	lepidolite	Rubikon	480	7	1.51	0.951	0.017	35.0	Step heating	Nice Sophia Antipolis
Lep-16-27	P74	lepidolite	Rubikon	468	7	1.55	0.927	0.018	35.5	Step heating	Nice Sophia Antipolis
Lep-16-27	P75	lepidolite	Rubikon	477	7	1.53	0.944	0.017	36.0	Step heating	Nice Sophia Antipolis
Lep-16-27	P76	lepidolite	Rubikon	488	7	1.51	0.968	0.017	36.5	Step heating	Nice Sophia Antipolis
Lep-16-27	P77	lepidolite	Rubikon	485	7	1.51	0.961	0.017	37.0	Step heating	Nice Sophia Antipolis
Lep-16-27	P78	lepidolite	Rubikon	473	7	1.54	0.937	0.017	37.5	Step heating	Nice Sophia Antipolis
Lep-16-27	P79	lepidolite	Rubikon	474	7	1.53	0.939	0.017	38.0	Step heating	Nice Sophia Antipolis
Lep-16-27	P80	lepidolite	Rubikon	478	7	1.51	0.948	0.017	38.5	Step heating	Nice Sophia Antipolis
Lep-16-27	P82	lepidolite	Rubikon	482	4	0.81	0.954	0.012	39.0	Step heating	Milano
Lep-16-27	P83	lepidolite	Rubikon	471	4	0.85	0.933	0.012	39.5	Step heating	Milano
<b>Weighted average age (Isoplot)</b>			<b>MSWD = 4.3</b>	<b>476</b>	<b>4</b>	<b>0.84</b>					
Lep-16-27-C	P85	lepidolite	Rubikon	493	8	1.54	0.977	0.017	46.3	Step heating	Nice Sophia Antipolis
Lep-16-27-C	P87	lepidolite	Rubikon	499	7	1.49	0.988	0.017	47.0	Step heating	Nice Sophia Antipolis
Lep-16-27-C	P88	lepidolite	Rubikon	484	7	1.53	0.960	0.017	47.5	Step heating	Nice Sophia Antipolis
Lep-16-27-C	P90	lepidolite	Rubikon	476	7	1.50	0.943	0.017	48.0	Step heating	Nice Sophia Antipolis
Lep-16-27-C	P92	lepidolite	Rubikon	500	7	1.49	0.990	0.017	48.5	Step heating	Nice Sophia Antipolis
Lep-16-27-C	P93	lepidolite	Rubikon	475	14	3.02	0.940	0.031	49.0	Step heating	Nice Sophia Antipolis
Lep-16-27-C	P94	lepidolite	Rubikon	502	8	1.50	0.994	0.017	49.5	Step heating	Nice Sophia Antipolis
Lep-16-27-C	P95	lepidolite	Rubikon	495	15	3.12	0.981	0.032	50.0	Step heating	Nice Sophia Antipolis
Lep-16-27-C	P97	lepidolite	Rubikon	505	8	1.49	1.000	0.017	50.5	Step heating	Nice Sophia Antipolis
Lep-16-27-C	P100	lepidolite	Rubikon	502	8	1.56	0.994	0.018	51.0	Step heating	Nice Sophia Antipolis
Lep-16-27-C	P101	lepidolite	Rubikon	485	7	1.49	0.960	0.017	51.5	Step heating	Nice Sophia Antipolis
Lep-16-27-C	P102	lepidolite	Rubikon	491	9	1.92	0.972	0.021	52.0	Step heating	Milano
<b>Weighted average age (Isoplot)</b>			<b>MSWD = 6.0</b>	<b>493</b>	<b>6</b>	<b>1.28</b>					

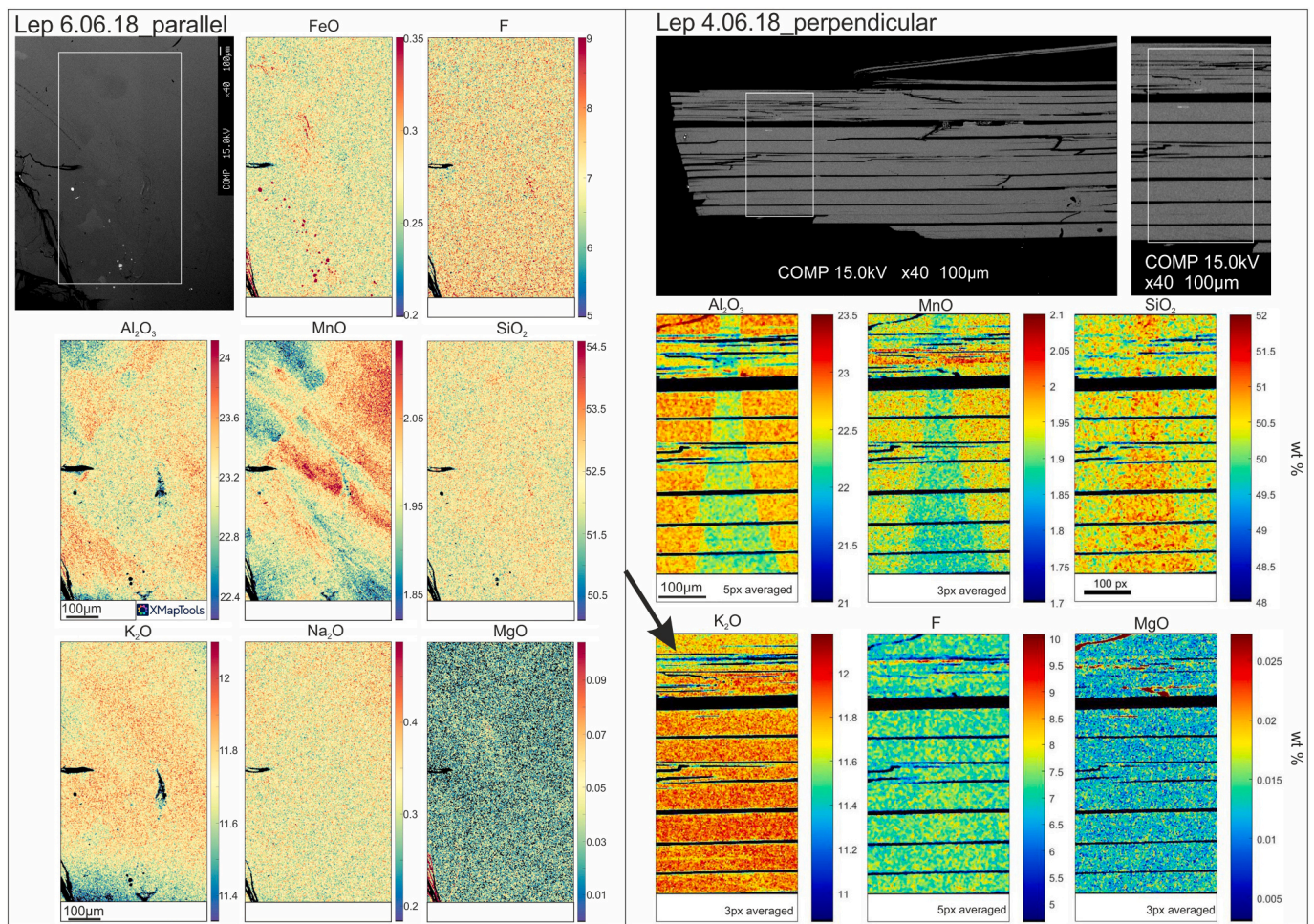


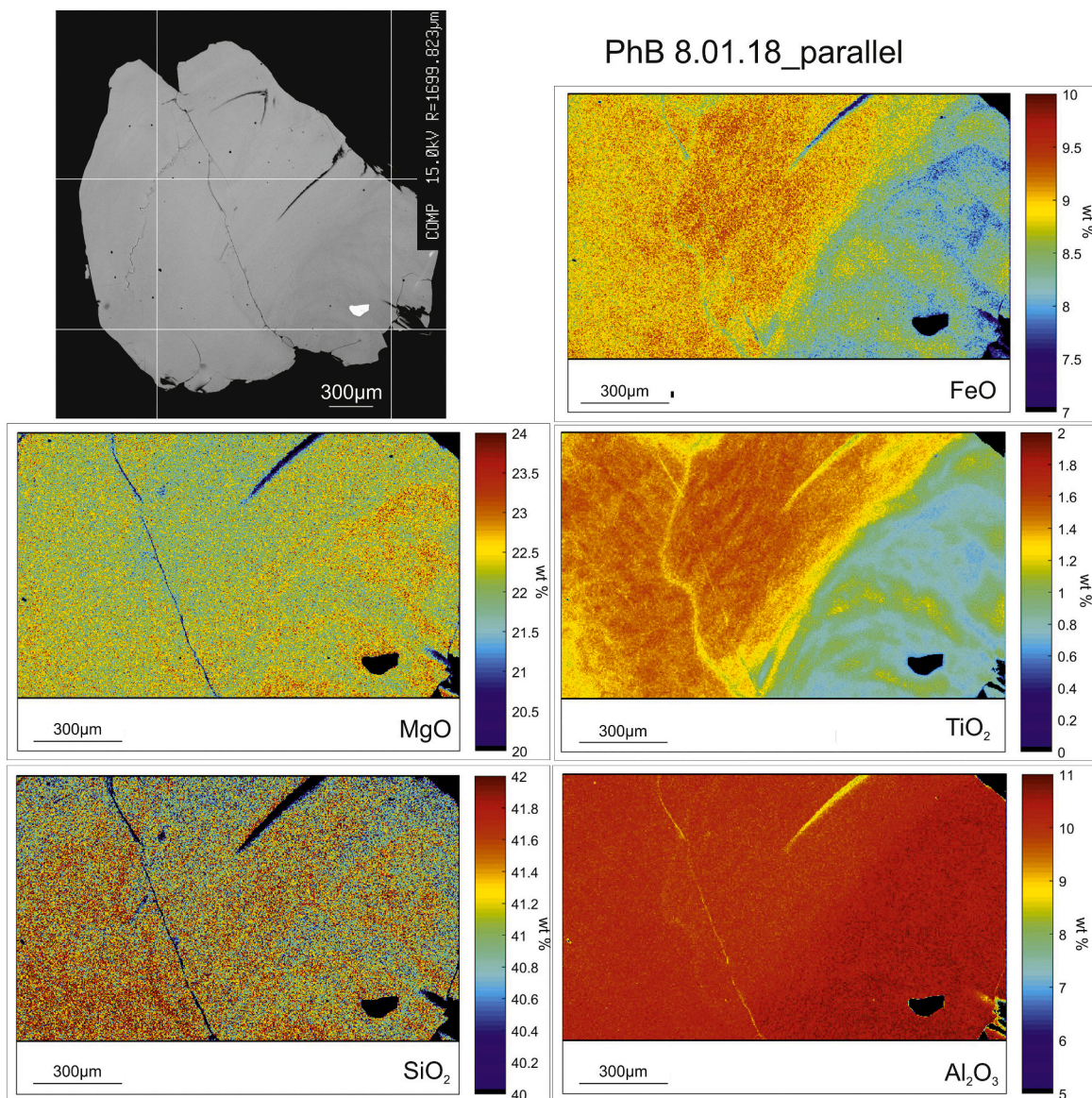
Fig. 3. Two examples of electron probe element maps of the Rubikón lepidolite, parallel and perpendicular to the (001) plane. Data treated with XMapTools, versions 2018 and 2020 (Lanari et al., 2014a, 2019). More element maps can be found in the Appendix B.

gaps (possibly enhanced by the polishing) are obvious, gaps being between 3 and 25  $\mu\text{m}$  thick; no gradual transition between the crystal and the gaps (where all element concentrations are zero) can be recognized. In addition, near the upper margin of the element map the lepidolite shows a prominent curved vertical feature rich in Si and poor in Al and Mn. It also shows an entire layer poorer in K and Al and slightly richer in F and Mn (arrow). The phlogopite (Fig. 4) shows the same (001)-parallel cleavages with lower element concentrations in the gaps; however, unlike lepidolite, Ti, Fe and Al (more insoluble elements) do not fall to zero like Mg and Si do. It appears that at least some cleavages were partly filled. This is more evident near the bottom of the element map (arrow), where in a 20  $\mu\text{m}$ -thick layer Mg reaches the double of the concentration it has in the rest of the map. In the plane parallel to (001), two microfractures are visible, one of them being totally unrelated to the 150% variation of the Ti concentration.

We interpret these observations as evidence that micas were affected by two processes: (1) fluid-assisted, open-system chemical reactions causing cation transport and element redistribution; (2) retrograde mineral formation. Some micas show signs of thin layers of vermiculite and/or pyrophyllite and/or talc developing in between mica sheets, even if initially a visual inspection by optical microscopy failed to reveal it. After EPMA element mapping had demonstrated mineral replacement, a dedicated re-investigation under the optical microscope did reveal some fuzzy darker bands that can reach 100  $\mu\text{m}$  width. As the element maps show that alteration is patchy at the mm scale, it is easy to explain why 100  $\mu\text{m}$  sized chips that were randomly cut across alteration patches showed haphazard ages. In the brighter and cleaner-looking

sheets the alteration bands are  $<5 \mu\text{m}$  wide. Alteration fronts are more likely to start along cracks, which favor the ingress of metasomatic fluids, which would cause younger ages near cracks. However, the presence of narrow (5  $\mu\text{m}$  wide) bands with anomalous element concentrations in the middle of mica sheets (Figs. 3-4) shows that the chemically open-system alteration followed three-dimensional pathways and did affect even chips that had seemed unaltered under an optical microscope. At a scale  $\approx 1 \text{ mm}$ , the heterogeneities are averaged away and only a slightly younger whole-grain plateau is recorded. The observation that Rb—Sr ages are close to the U—Pb ages was used by Naumenko-Dèzes et al. (2018) to hypothesize that the geochemically similar K—Ca parent-daughter pair likely also should give an age concordant with the U—Pb age. From the assumed K—Ca age and the measured  $^{40}\text{Ca}^*/^{40}\text{K}$  ratio they constrained the half-life and branching ratio of the  $^{40}\text{K}$  decay. The closed behaviour of the Rb—Sr system despite the introduction of Mg and Ti (which requires at least local recrystallization of the T-O-T mica framework hosting Mg and Ti) suggests that the earth-alkali daughter isotopes  $^{87}\text{Sr}^*$  and  $^{40}\text{Ca}^*$  are reprecipitated into the recrystallizing vermiculite/talc pseudomorph, whereas incompatible  $^{40}\text{Ar}^*$  daughter isotopes are lost, giving the rejuvenated K—Ar ages presented here. This agrees with the common observation that newly-formed crystals in presence of fluids do not retain any excess or inherited argon (e.g., Sanchez et al., 2011).

We sought the causes of the age discordance among the samples for those chips whose  $^{38}\text{Ar}_{\text{Cl}}$  signal was sufficiently well-resolved from the background, i.e., those nine with a sample mass  $> 0.18 \text{ mg}$ . We also obtained a detectable  $^{37}\text{Ar}$  signal on three samples measured within two



PhB 8.01.18\_perpendicular

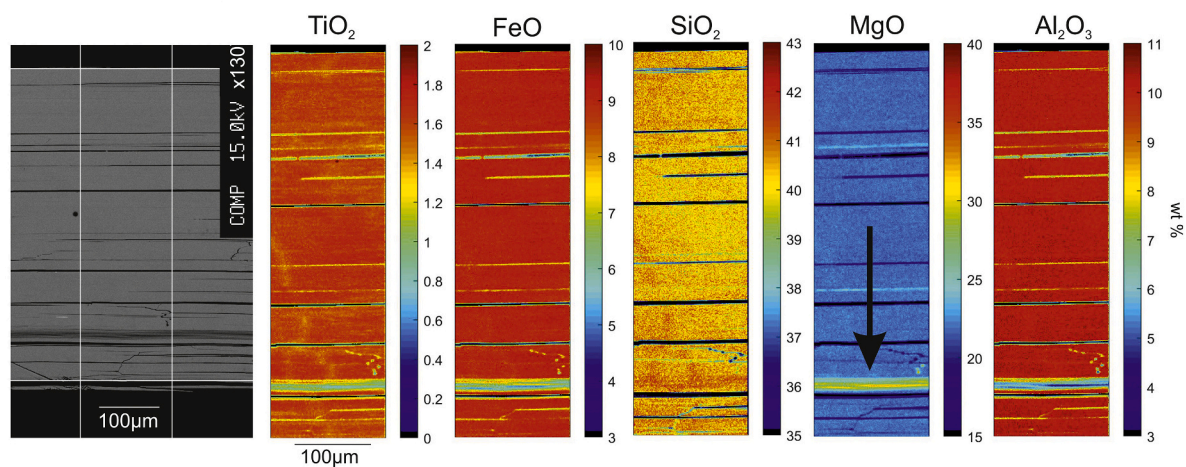


Fig. 4. Two examples of electron probe element maps of the Phalaborwa phlogopite, parallel and perpendicular to the (001) plane. Data treated with XMapTools (Lanari et al., 2014a, 2019). More element maps can be found in the Appendix B

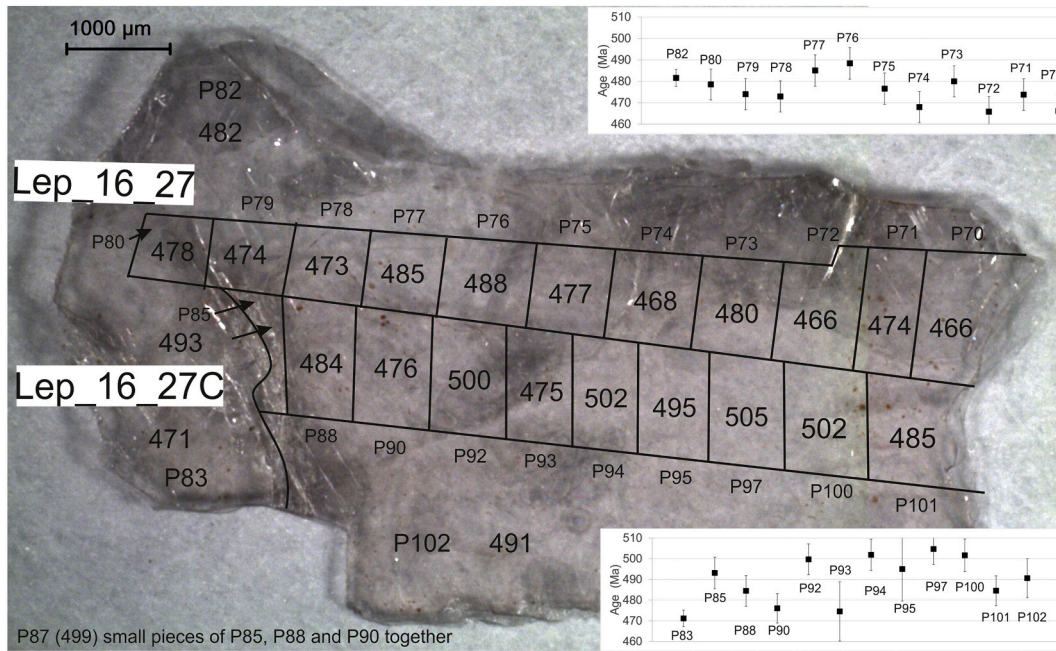


Fig. 5. Apparent  $^{40}\text{Ar}/^{39}\text{Ar}$  ages of Rubikon lepidolite chips, normalized to chip P97 assumed to have an age equal to the Rb–Sr age.

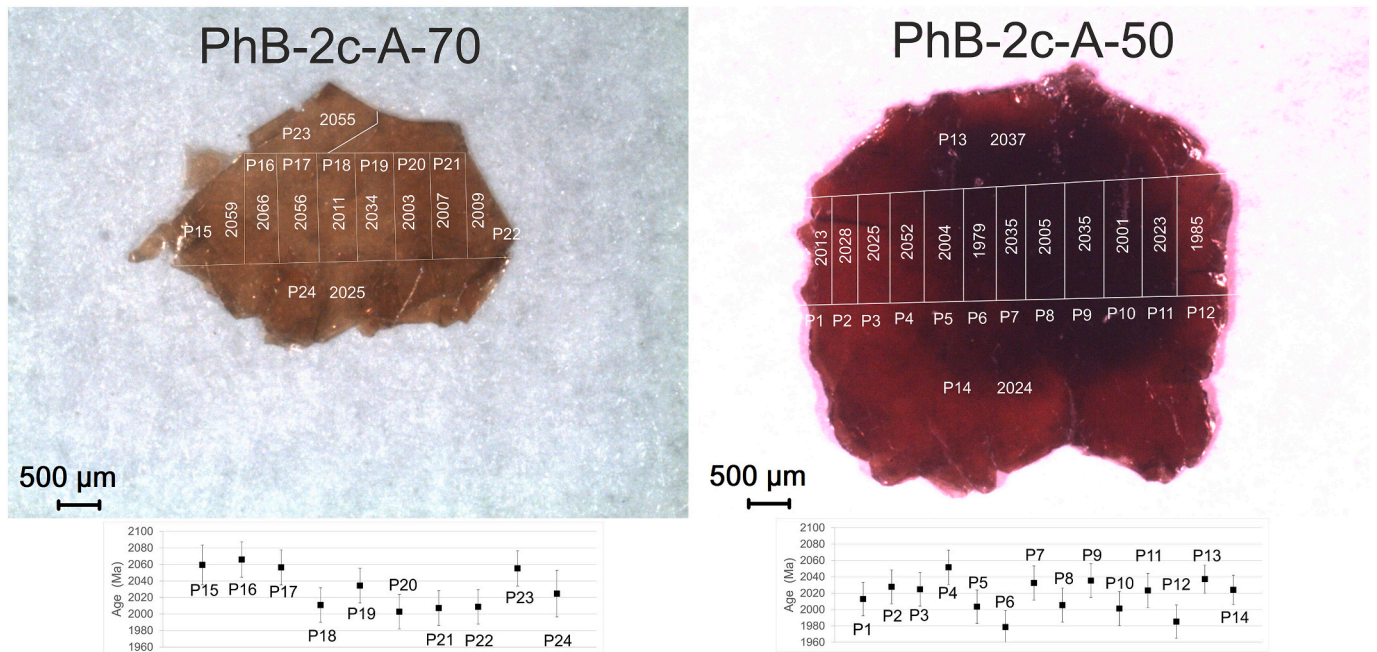


Fig. 6. Apparent  $^{40}\text{Ar}/^{39}\text{Ar}$  ages of Phalaborwa phlogopite chips, normalized to chip P67 assumed to have an age equal to the Rb–Sr age.

months of irradiation. The Ca/K ratios are highest in the low temperature steps, which we attribute to heterochemical retrogression phases, and decrease by 2–3 orders of magnitude in the steps representing the degassing of the micas *sensu stricto*. Two Phalaborwa samples had identical Ca/K ratios of  $0.0018 \pm 0.0003$  (P14) and  $0.0017 \pm 0.0009$  (P32) in the isochemical steps (the steps in which the Cl/K ratio (and the Ca/K ratio, where available) shows a constant chemical signature); the isochemical steps of one Rubikon sample averaged  $\text{Ca}/\text{K} = 0.0031 \pm 0.0008$ . In the three studied instances, the Ca/K ratios of the isochemical steps show no correlation with the corresponding ages.

Where the  $^{38}\text{Ar}_{\text{Cl}}$  and  $^{37}\text{Ar}_{\text{Ca}}$  are well resolved from background we

can investigate isochemical ages (as defined by [Villa et al., 2006](#)), i.e., the average of ages in the isochemical steps; normally isochemical steps yield indistinguishable ages ([Villa and Hanchar, 2017](#)), as they do here. The steps with a constant Cl/K ratio in the Phalaborwa and Rubikon samples are those with the lowest Cl/K. In contrast, the first step degassed at low temperature always showed high Cl/K, 1–2 orders of magnitude higher than the isochemical steps. The age of the first step is generally younger. The negative correlation between age and Cl/K ratio is statistically significant at the 95% confidence level only in few cases (Appendix C), even if it appears ubiquitous. Because of this correlation trend, in principle the most reliable estimate of the K–Ar age is not

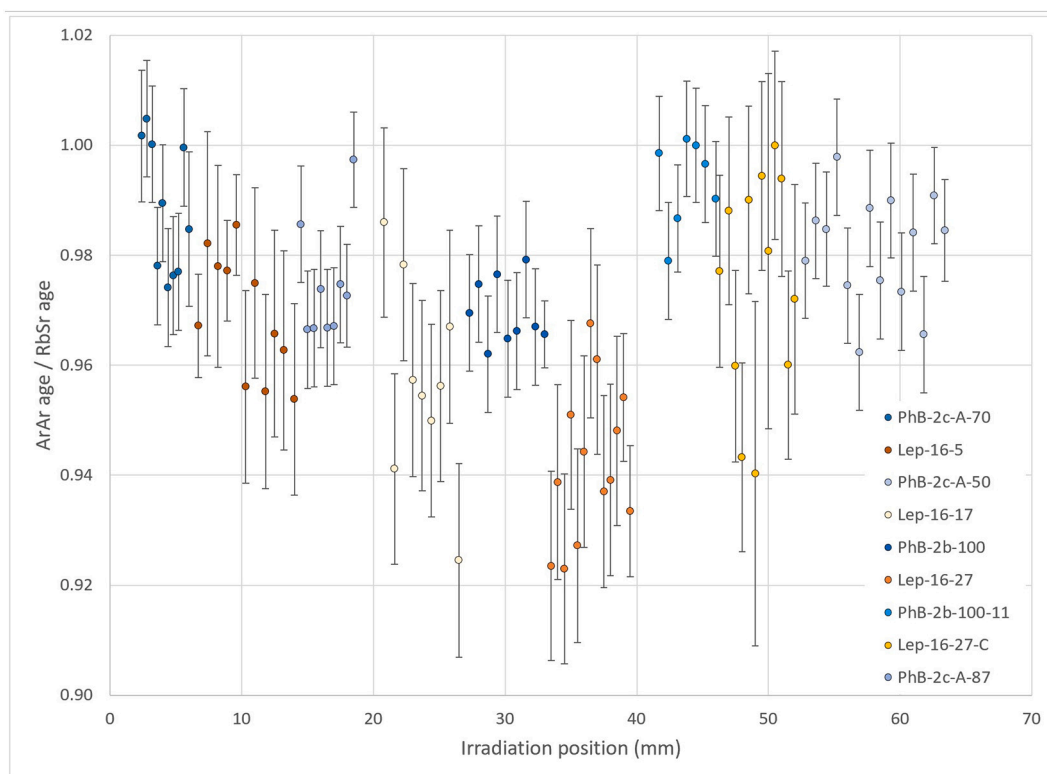


Fig. 7. Normalized (self-monitored) age vs. position of rectangular chips in the irradiation canister.

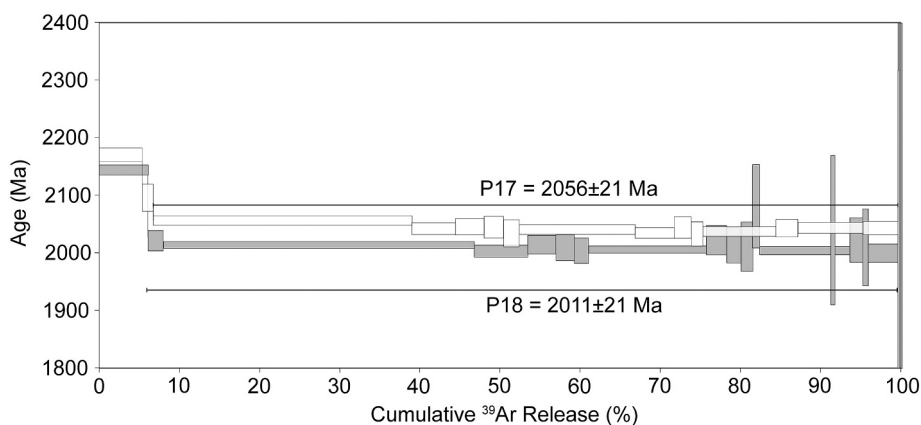


Fig. 8. “Plateau” ages for two neighboring chips of the Phalaborwa phlogopite. The height of the boxes is the 2 sigma uncertainty of each step.

given by the “plateau” age but by the leftmost (Cl-poorest) end-point of the Cl/K-age alteration trend, even if in practice the two coincide. However, as clear as the petrochronological evidence may be, neither the Phalaborwa phlogopite nor the Rubikon lepidolite are suitable as decay constant calibrators for the K—Ar system, as the extrapolated correction of their measured apparent ages to model the “pre-alteration” K—Ar ages entails possible systematic errors exceeding 1%.

By inference, this conclusion should be applied to all cases where no conclusive proof of the absence of retrogression was provided. The stratigraphic and geodynamic modeling at the km scale should always take into account the physical and chemical phenomena occurring at the sub- $\mu\text{m}$  scale (Villa, 2006; Hochella Jr., 2008; Ju et al., 2020, and references therein).

#### 4. Conclusions

This study demonstrates a previously neglected phenomenon: even “rapidly cooled”, clear, visually unaltered, museum-grade micas can be incompletely pristine geochronometers. In particular, small (5  $\mu\text{m}$  wide) alteration layers between mica sheets already can affect K—Ar ages by several percent if the analyzed chip is small enough. Large variations of the Ti and Mg concentrations are signs of retrograde reactions that correspond to the large K—Ar age variations. Step heating “plateaus”, as were obtained for all the samples in this study, do not guarantee that the K—Ar system was not partially reset. The spatial distribution of the apparent ages of subgrain chips does not support the idea that K—Ar ages only represent cooling ages. The present study documents subtle, patchy open-system compositional changes, which were detected by electron microprobe. This chemical heterogeneity requires one or more episodes of mass transfer mediated by post-magmatic aqueous fluid

circulation.

The diagnostic tools that the  $^{40}\text{Ar}/^{39}\text{Ar}$  systematics provide are a judicious use of the isotope correlation plots, especially the Cl/K-age and Ca/K-age diagrams. Identifying trends and extrapolating them to an end-member composition can provide a correction for the effects of metasomatism and alteration, but the precision of the extrapolation is limited by the precision of the electron probe microanalysis that constrains the pristine chemical composition of the unaltered patches. The potential to use the intercomparison of mineral ages as a calibration of half-lives suffers from the same limitation on precision.

### Declaration of Competing Interest

The authors declare that they have no known competing financial interests or personal relationships that could have appeared to influence the work reported in this paper.

### Acknowledgements

Samples were donated by K. Mezger and B.A. Hofmann. Funding for M.O.N.-D. were provided by the Schweizerische Nationalfonds, grants 200021-131916 and 200020-153126. Analyses in Nice Sophia Antipolis were supported by a Géoazur internal fund. Valentina Barberini (Milano Bicocca) is thanked for laboratory maintenance. Reviews by Anonymous, D.V. Popov and B.S. Kamber greatly improved the manuscript.

### Appendix A. Supplementary data

Supplementary data to this article can be found online at <https://doi.org/10.1016/j.chemgeo.2021.120215>.

### References

- Bachmann, O., Dungan, M.A., Lipman, P.W., 2002. The Fish Canyon magma body, San Juan volcanic field, Colorado: rejuvenation and eruption of an upper-crustal batholith. *J. Petrol.* 43, 1469–1503.
- Begemann, F., Ludwig, K.R., Lugmair, G.W., Min, K.W., Nyquist, L.E., Patchett, P.J., Renne, P.R., Shih, C.Y., Villa, I.M., Walker, R.J., 2001. Call for an improved set of decay constants for geochronological use. *Geochim. Cosmochim. Acta* 65, 111–121.
- Bosio, G., Malinverno, E., Villa, I.M., Di Celma, C., Gariboldi, K., Giocada, A., Barberini, V., Urbina, M., Bianucci, G., 2020. Tephrochronology and chronostratigraphy of the Miocene Chilcatay and Pisco formations (East Pisco Basin, Peru). *Newsl. Stratigr.* 53, 213–247.
- Cebula, G.T., Kunk, M.J., Mehnert, H.H., Naeser, C.W., Obradovich, J.D., Sutter, J.F., 1986. The Fish Canyon tuff, a potential standard for the  $^{40}\text{Ar}/^{39}\text{Ar}$  and fission-track methods. *Terra Cognita* 6, 139–140.
- Dèzes, M., 2016. Refined isotopic compositions of K, Ca and a complementary comparison of the 40K-40Ca, 40K-40Ar and 87Rb-87Sr chronometers. Doctoral dissertation, Universität Bern. Chapter 3.
- Flude, S., Halton, A.M., Kelley, S.P., Sherlock, S.C., Schwaneethal, J., Wilkinson, C.M., 2014. Observation of centimetre-scale argon diffusion in alkali feldspars: implications for 40Ar/39Ar thermochronology. *Geol. Soc. Lond. Spec. Publ.* 378, 265–275.
- Foland, K.A., 1983.  $^{40}\text{Ar}/^{39}\text{Ar}$  incremental heating plateaus for biotites with excess argon. *Chem. Geol.* 41, 3–21.
- Heri, A.R., Robyr, M., Villa, I.M., 2014. Petrology and geochronology of the “muscovite standard” B4M. In: Jourdan, F., Mark, D., Verati, C. (Eds.),  $^{40}\text{Ar}/^{39}\text{Ar}$  Dating: from Geochronology to Thermochronology, from Archaeology to Planetary Sciences. Geological Society London Special Publication, 378, pp. 69–78.
- Hochella Jr., M.F., 2008. Nanogeoscience: from origins to cutting-edge applications. *Elements* 4, 373–379.
- JCGM - Joint Committee for Guides in Metrology, 2008. Guide to the expression of uncertainty in measurement. [www.bipm.org/en/publications/guides/gum.html](http://www.bipm.org/en/publications/guides/gum.html).
- Jicha, B.R., Singer, B.S., Sobol, P., 2016. Re-evaluation of the ages of  $^{40}\text{Ar}/^{39}\text{Ar}$  sanidine standards and supereruptions in the western US using a Noblesse multi-collector mass spectrometer. *Chem. Geol.* 431, 54–66.
- Ju, Y.W., Wan, Q., Hochella Jr., M.F., 2020. Editorial for special issue “Nanomineralogy”. *Minerals* 10, 520.
- Koppers, A.A., 2002. ArArCALC—software for  $^{40}\text{Ar}/^{39}\text{Ar}$  age calculations. *Comput. Geosci.* 28 (5), 605–619.
- Kumar, A., Nagaraju, E., Sarma, D.S., Davis, D.W., 2014. Precise Pb baddeleyite geochronology by the thermal extraction-thermal ionization mass spectrometry method. *Chem. Geol.* 372, 72–79.
- Lanari, P., Vidal, O., De Andrade, V., Dubacq, B., Lewin, E., Grosch, E.G., Schwartz, S., 2014a. XMapTools: a MATLAB®-based program for electron microprobe X-ray image processing and geothermobarometry. *Comput. Geosci.* 62, 227–240.
- Lanari, P., Rolland, Y., Schwartz, S., Vidal, O., Guillot, S., Tricart, P., Dumont, T., 2014b. P–T estimation of deformation in low-grade quartz-feldspar-bearing rocks using thermodynamic modelling and 40Ar/39Ar dating techniques: example of the Plan-de-Phasy shear zone unit (Briançonnais Zone, Western Alps). *Terra Nova* 26 (2), 130–138.
- Lanari, P., Vho, A., Bovay, T., Airaghi, L., Centrella, S., 2019. Quantitative compositional mapping of mineral phases by electron probe micro-analyser. *Geol. Soc. Lond., Spec. Publ.* 478 (1), 39–63.
- Melcher, F., Graupner, T., Gäbler, H.-E., Sitnikova, M., Henjes-Kunst, F., Oberthür, T., Gerdes, A., Dewaele, S., 2015. Tantalum-niobium-tin mineralisation in African pegmatites and rare metal granites: Constraints from Ta-Nb oxide mineralogy, geochemistry and U-Pb geochronology. *Ore Geol. Rev.* 64, 667–719.
- Nägler, T.F., Villa, I.M., 2000. In pursuit of the  $^{40}\text{K}$  branching ratio: K-Ca and  $^{39}\text{Ar}/^{40}\text{Ar}$  dating of gem silicates. *Chem. Geol.* 169, 5–16.
- Naumenko-Dèzes, M.O., Nægler, T.F., Villa, I.M., Mezger, K., 2018.  $^{40}\text{K}/^{40}\text{Ca} - ^{87}\text{Rb}/^{87}\text{Sr}$  age comparison: constraints on the  $^{40}\text{K}$  decay constant. *Geochim. Cosmochim. Acta* 220, 235–247.
- Popov, D.V., Brovchenko, V.D., Nekrylov, N.A., Plechov, P.Y., Spikings, R.A., Tyutyunnik, O.A., Krigman, L.V., Anosova, M.O., Kostitsyn, Y.A., Soloviev, A.V., 2019. Removing a mask of alteration: geochemistry and age of the Karadag volcanic sequence in SE Crimea. *Lithos* 324, 371–384.
- Rivera, T.A., Storey, M., Zeeden, C., Hilgen, F.J., Kuiper, K., 2011. A refined astronomically calibrated  $^{40}\text{Ar}/^{39}\text{Ar}$  age for Fish Canyon sanidine. *Earth Planet. Sci. Lett.* 311, 420–426.
- Sanchez, G., Rolland, Y., Schneider, J., Corsini, M., Olliot, E., Goncalves, P., Verati, C., Lardeaux, J.M., Marquer, D., 2011. Dating low-temperature deformation by  $^{40}\text{Ar}/^{39}\text{Ar}$  on white mica, insights from the Argentera-Mercantour Massif (SW Alps). *Lithos* 125, 521–536.
- Steiger, R.H., Jäger, E., 1977. Subcommittee on geochronology: convention on the use of decay constants in geo- and cosmochronology. *Earth Planet. Sci. Lett.* 36, 359–362.
- Villa, I.M., 2006. From the nm to the Mm: isotopes, atomic-scale processes, and continent-scale tectonic models. *Lithos* 87, 155–173.
- Villa, I.M., 2016. Diffusion in mineral geochronometers: present and absent. *Chem. Geol.* 420, 1–10.
- Villa I.M., De Bièvre P., Holden N.E., Renne P.R., 2015. IUPAC-IUGS recommendation on the half life of 87Rb. *Geochim. Cosmochim. Acta* 164, 382–385.
- Villa, I.M., Hancher, J.M., 2017. Age discordance and mineralogy. *Am. Mineral.* 102, 2422–2439.
- Villa, I.M., Ruggieri, G., Puxeddu, M., Bertini, G., 2006. Geochronology and isotope transport systematics in a subsurface granite from the Larderello-Travale geothermal system (Italy). *J. Volcanol. Geotherm. Res.* 152, 20–50.
- Villa, I.M., Bonardi, M.L., De Bièvre, P., Holden, N.E., Renne, P.R., 2016. IUPAC-IUGS status report on the half-lives of  $^{238}\text{U}$ ,  $^{235}\text{U}$  and  $^{234}\text{U}$ . *Geochim. Cosmochim. Acta* 172, 387–392.
- Villa, I.M., Holden, N.E., Possolo, A., Hibbert, D.B., Ickert, R.B., Renne, P.R., 2020. IUGS-IUPAC recommendation on the half-lives of  $^{147}\text{Sm}$  and  $^{146}\text{Sm}$ . *Geochim. Cosmochim. Acta* 285, 70–77.
- Wu, F.Y., Yang, Y.H., Li, Q.L., Mitchell, R.H., Dawson, J.B., Brandl, G., Yuhara, M., 2011. *In situ* determination of U–Pb ages and Sr–Nd–Hf isotopic constraints on the petrogenesis of the Phalaborwa carbonatite complex, South Africa. *Lithos* 127, 309–322.